An actuator–sensor hybrid device made of carbon-based polymer composite for self-sensing systems

An actuator–sensor hybrid device made of carbon-based polymer composite for self-sensing systems

Cite as: AIP Advances 9, 065311 (2019); doi: 10.1063/1.5100110
Submitted: 15 April 2019 • Accepted: 22 May 2019 •
Published Online: 14 June 2019

Atsushi Nakamura[a] and Shotaro Kawakami

AFFILIATIONS

Graduate School of Integrated Science and Technology, Shizuoka University, 3-5-1 Johoku, Hamamatsu, Shizuoka 432-8011, Japan

[a]Corresponding author. Email: nakamura.atsushi@shizuoka.ac.jp

ABSTRACT

This paper presents the concept, design, and characterization of a new type of integrated device with a hybrid structure. The proposed device is hybridized with an electrothermal actuator and a bending sensor with temperature-compensating ability, which can serve as a self-sensing system. The sensor displays a parallel change in the electrical resistance upon the temperature alteration, resulting enables a cancellation of cross talk. The actuator exhibits a visible maximum strain of 1.2% at an electric power intensity of around 1.05 mW/mm^3, and the bending sensor can display the curvature without the need for an external monitoring system such as a laser displacement meter. The traceability of the motion is represented well while power is supplied, but a slight delay occurs when the power is switched off, this being due to the difference in thermal conductivity between the composite of the actuator and the sensor. This proposed hybrid device realizes a simple self-sensing operation using a simple power supply and monitoring reading lines. It offers ease of fabrication and promising practical applications in remote sensing/operating devices.

I. INTRODUCTION

Electroactive polymers (EAPs) have great potential as soft actuators in applications such as soft robotics,[1–3] artificial muscles,[4–7] switches,[8,9] microsensors,[7,10] and biomimetic devices.[1,4,6,10,11] Numerous studies have been conducted and applications realized based on the facts that EAPs (i) provide large-strain polymorphic actuation when driven by an electric field or current, (ii) have the advantages of being cheap, lightweight, and easy to control and permitting facile fabrication,[12–15] and (iii) can be used in air.[12–15]

Recently, among EAPs, electrothermal actuators (ETAs) have progressed steadily in response to requirements for flexible, agile, and complex actions.[12–18] By using a matrix of waterborne polyurethane or polydimethylsiloxane (PDMS), Zeng *et al.* achieved very considerable bending displacement with an ultra-low direct-current (DC) driving voltage (<7 V) and a low power density (<25 mW/mm^3).[16] Li *et al.* demonstrated functional electrothermal bimorph actuators that are capable of substantial bending deformations and bionic movements when driven by electricity.[18] However, despite the fact that actuators can perform biomimetically agile or complex actions, the actuation motion itself is measured by traditional cameras, laser displacement sensors, laser-sight infrared thermometers, and infrared thermal imagers.[12–18] Therefore, these devices have the lack of a feedback system for their positions, motions, and sensory of temperature compensation. Integrating an actuator and its sensors in a self-sensing system remains a challenge, and there have been relatively few studies of self-sensing for responsive actuation.[19–21]

The ETAs of a bimorph structure perform bending actuation because of a mismatch in the coefficients of thermal expansion between two materials.[16] Joule heat is generated by the current through the conductive layer when a voltage is applied, and hence the whole bimorph layers are heated up and transfer heat to the counter layer.[16] The relationship between the accurate temperature transferred onto the interface and the input power density is important for sensory feedback to realize biomimetic actions. A temperature sensor that can be embedded or attached to an actuator is required instead of an external radiation temperature sensor.

Additionally, in current techniques, image processing by a camera or a video recorder is required to observe the bending motion of the actuator, and that can make the system complex and increase the processing time.

Recently, Amjadi and Sitti demonstrated multi-responsive actuators comprising normal copy paper and polypropylene film with a sensing function.[21] They realized independent electrothermal simulation and real-time displacement sensors by hybridizing graphite microparticles and carbon nanotubes (CNTs), and they used a hybrid film to adjust the nearly-zero thermal coefficient of resistance (TCR) of the piezoresistive sensor because of the opposite change in the electrical resistance upon the temperature alteration and bending of the actuator.

Here, we propose an integrated device with a hybrid structure of an electrothermal actuator and a bending sensor with temperature-compensating ability, which can serve as a self-sensing system. The base of the actuator is a bimorph structure comprising a multiwalled CNT/PDMS composite and PDMS. The bending sensor is a cylindrical hollow-tube structure comprising graphene fibers with PDMS, which we reported previously[22] and is attached to the actuator surface to detect the bending curvature and temperature. The difference between the previous self-sensing concept[21] and the present one is the piezoresistive sensor and the hybrid structure including the sensor properly. The piezoresistive sensor comprises the same PDMS matrix for the actuator, one that can measure the accurate temperature on one side of the PDMS layer of the actuator. Furthermore, the advantage of the present work is that the piezoresistive bending sensor displays a parallel change in the electrical resistance upon the temperature alteration, resulting enables a cancellation of cross talk. The proposed hybrid device will be helpful for remote sensing/operating devices.

II. EXPERIMENTAL DETAILS

A. Materials

Nickel (Ni) wires (purity 99.99%) and aluminum (Al) wires (purity 99.99%) were purchased from the Nilaco Corporation of Japan; the diameters of the Ni wires were 0.2 mm and 0.5 mm, and that of the Al wires was 0.2 mm. A Ni oxide removal agent (Nickel selective etchant-NC) and a Ni etchant (Ni etchant-H) were purchased from the Nihon Kagaku Sangyo Co., Ltd. of Japan. Sylgard 184 (prepolymer of poly(dimethylsiloxane) (PDMS) and catalyst) was purchased from Dow Corning Toray. (Tokyo, Japan). The rigidity of the PDMS was controlled by the concentration of cross-linker agent in the base PDMS solution and by the baking temperature and time. Multiwalled CNTs (MWCNTs) were purchased from EM Japan Co., Ltd. (G-24) with typical lengths of 1–50 nm and diameters of 50–85 nm.

B. Actuator/bending-sensor preparation

Details of the fabrication process of the MWCNT/PDMS composite and PDMS bimorph actuators are shown in Fig. S1 (in supplementary material). Briefly, the bimorph structure comprised an MWCNT/PDMS composite layer that was laminated on the PDMS layer. The typical electrical resistivity of the 15 wt% MWCNT/PDMS was around 1 kΩ·cm, which was measured by a van der Pauw configuration. Two of the Ni wires were embedded in the interface between the MWCNT/PDMS composite layer and the PDMS layer to enhance the conduction of the applied current homogeneously. Details of the fabrication process of the graphene/PDMS piezoresistance bending sensor are shown in Fig. S2. Briefly, it comprised a hollow tube of graphene fibers surrounded by a PDMS thin-film coating. The graphene fibers for the tube were obtained via etching from graphene layers grown by chemical vapor deposition on Ni fibers. Raman spectra were used to confirm that the graphene fibers had a graphite structure (see Fig. S3).

Figure 1 shows an overview of the hybrid actuator–sensor device structure; Fig. 1(a) shows a photograph of the device and Fig. 1(b) shows a schematic of the MWCNT/PDMS-composite/PDMS actuator and the sensor. The bending sensor was attached on the PDMS side of the actuator with a small amount of PDMS that was then cured to set the sensor. The proposed integrating device for the electrothermal actuator and the bending sensor was basically formed by the same materials. Therefore, the temperature and bending curvature are assumed to be accurate. The typical size of the device was 52 mm × 16 mm (length × width) with a typical thickness of around 2.5 mm. Figure 1(c) shows a schematic of the actuator bending into an arc. Considering the bending curvature of the actuator, the following equations were used to evaluate the displacement. Thus, we have $cos\theta = (r-d)/r$ and $\theta = l/r$, where θ is the

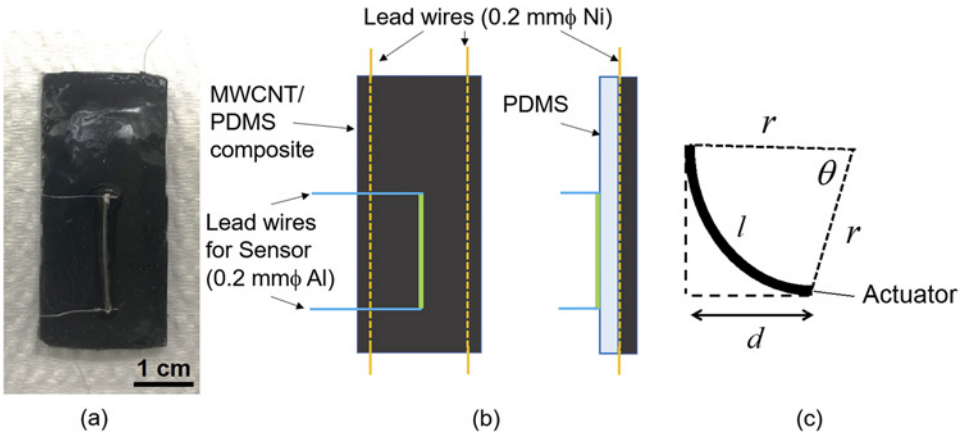

FIG. 1. Overview of device structure in actuator–sensor hybrid: (a) photograph; (b) schematic of MWCNT/PDMS-composite/PDMS actuator and sensor; (c) schematic of actuator bending into an arc.

angle of the arc, r is the radius of curvature, d is the displacement of the free end of the actuator, and l is the length of the arc. Therefore, the displacement d can be derived by solving $d = r(1 - \cos(l/r))$ numerically.

C. Characterization

Raman spectroscopy (NRS-7000; Jasco, USA) with a laser excitation wavelength of 532 nm was used to evaluate the crystalline quality and uniformity of the graphene. The temperature of the actuator was measured with an infrared thermal camera (FLIR C2; FLIR, USA) with a temperature resolution of 100 mK. The electrical conductivity was measured with a semiconductor characterization system (model 4200-SCS; Keithley, USA). The static characterization of the resistance variation with temperature was carried out while monitoring the temperature of a sample placed on a hot plate (RSH-1DN; AS ONE Corp., Japan). The electro-mechanical test was performed by measuring the resistance change ($\Delta R/R_0$) while a mechanical tensile strain was applied to the sample by a hand-made tensile testing machine and a hand-made bending testing machine. The tensile strain test was conducted using a digital force gauge (DS2-50N; IMADA Co. Ltd., Japan); the deformation was captured by a digital camera and the images were analyzed using image analysis software (ImageJ; NIH, USA). Testing bend sensors were attached to the plastic plate holder to fold, and the bending angle was adjusted by a hand while observing a simplified protractor.

III. RESULTS AND DISCUSSION

Figure S1(d) shows photographs of the suspended actuator before and after a 35 V DC voltage was applied to drive it. One end of the actuator was fixed and the other end could bend toward the MWCNT/PDMS side in the atmosphere under the applied DC voltage. The actuator bent with an applied voltage of 35 V is shown in Fig. 2(a). The maximum displacement was 14.4 mm (with a curvature of 0.187 cm^{-1}) after 14 s. The tip of the actuator returned to the initial position around 86 s after the power source was switched off. The inset of Fig. 2(a) shows enlarged scales for both time and displacement. This indicates that the actuator started to bend in the opposite direction for a few seconds after the power-source voltage of 35 V was applied, whereupon the actuator bent toward the PDMS side. The actuation mechanism is considered as follows. Joule heat is generated by the current through the conductive MWCNT paths in the PDMS matrix when the voltage is applied. The MWCNT/PDMS composite film heats up immediately and transfers heat to the PDMS film. As the temperature of the entire actuator rises, so the actuator expands because of the thermal expansion of the polymer matrix. In the preliminary stage, the PDMS layer expands more than does the MWCNT/PDMS composite because of the higher coefficient of thermal expansion of the former, resulting in bending toward the MWCNT/PDMS direction. As the temperature rises further, the actuator bends in the reverse direction because of the higher Young's modulus of the latter. Figure 2(b) shows the stress–strain curves of pure PDMS and the MWCNT/PDMS composite film at room temperature. These exhibit the typical linear elastic region for strains up to 20%. The values of Young's modulus (E) for PDMS and MWCNT/PDMS were obtained from the slope of the linear region and were 0.65 and 1.13 MPa, respectively. Additionally, the values of the coefficient of thermal expansion for PDMS and MWCNT/PDMS were 8.3 and 5.8 μm/K, respectively.

Next, the magnitude of the piezoresistive effect in the as-fabricated graphene-tubing bending sensor was investigated by monitoring its resistance with known curvature ρ in the range of 0–10.3 m^{-1}. The gauge factor (GF) is a common index for explaining the sensitivity of electrical shift to mechanical deformation and was calculated as approximately 9.43 from the tensile strain converted from the curvature (see Fig. S4). Figure 3(a) shows a plot of $\Delta R/R_0$ versus time under a cyclic bending curvature of 5 m^{-1}, and Fig. 3(b) shows a plot of the mean of $\Delta R/R_0$ with error bars for the standard deviation. To investigate the repeatability of the bending sensor, its coefficient of variation was calculated for a repeated response of the sensor through a range of cycles. The calculated coefficient of variation is less than approximately 10%, indicating that

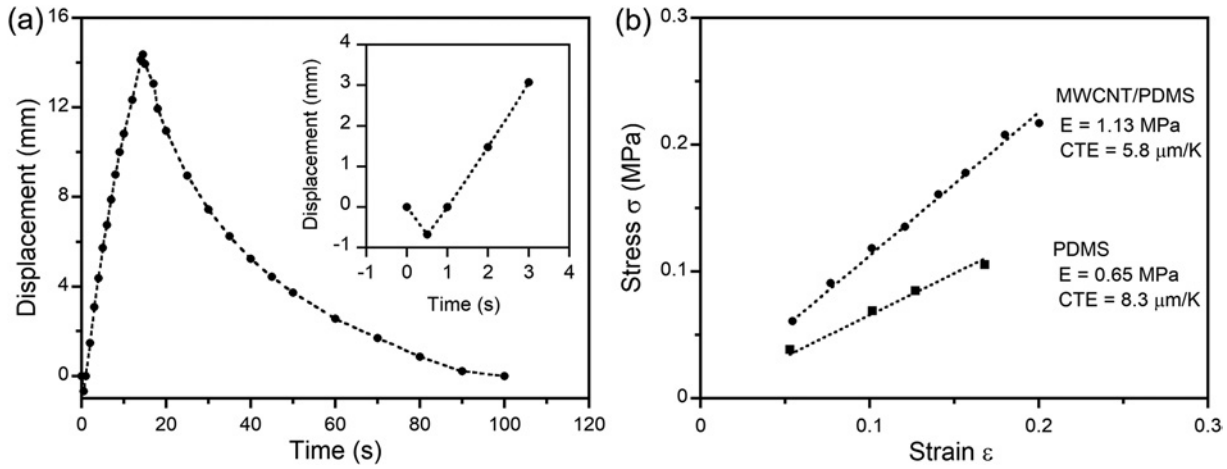

FIG. 2. (a) Displacement variation of MWCNT/PDMS-composite/PDMS bimorph actuator with an applied DC voltage of 35 V and a current of 198.6 mA. The inset shows enlarged scales for both time and displacement. (b) Stress–strain curves of pure PDMS and MWCNT/PDMS composite film at room temperature.

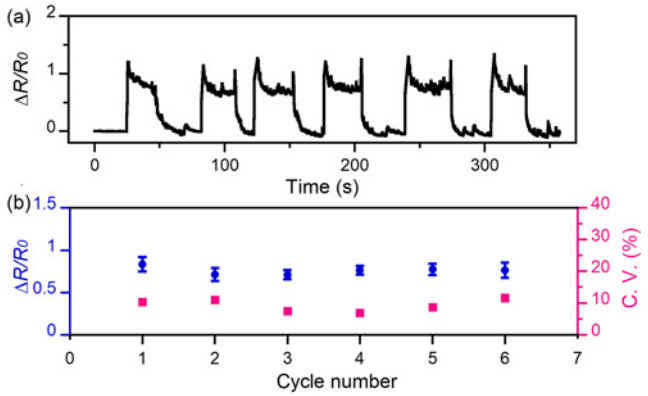

FIG. 3. (a) Relative resistance change versus time under repeated bending at a bending curvature of 5 m^{-1}. (b) Relative resistance change and coefficient of variation as a function of cycle number.

the sensor has good sensing performance. The thermal stability of the graphene-tubing bending sensor was characterized in previous work,[22] indicating excellent stability with a signal-to-noise ratio of 37.7 dB. Figure 4(a) shows how the curvature of the bending sensor varies with the relative resistance. A nearly linear relationship between resistance change and curvature was obtained in the range between 0 and 3 m^{-1}. The nonlinear relationship for curvatures of 3–8 m^{-1} is due to the tube deforming because of a larger bending angle. However, the linear trend returns when the curvature exceeds 8 m^{-1} since the tube is fully suppressed. The relationship between the curvature and the relative resistance is

$$\rho = 4.159 \times \Delta R/R_0. \tag{1}$$

In a further sensing study for the temperature, the relative resistance variation of the sensor was investigated with no applied strain. The temperature was determined in accordance with an electrical hotplate monitor. The device resistance depends on the conduction electrons by increasing the temperature and their mobility will be decreased. The relative resistance of the bending sensor for temperatures of 298–333 K normalized by the resistance at 298 K is shown in Fig. 4(b). The measured data were fitted by the dotted lines in Fig. 4(b), showing a quadratic dependence of resistance on temperature that is similar to thermistor (semiconductor) behavior.[23] The resistance change is proportional to T^2, and the fitting curve is

$$\Delta R/R_0 = 28.568 - 0.2012T + 0.00035342T^2. \tag{2}$$

When an actuator is heated, the change in the electrical resistance of the attached bending sensor is determined by summarizing the temperature dependence of its resistance and its piezoresistive response to the induced mechanical strain during bending deformation of the actuator. The temperature-dependent resistance change of the bending sensor interferes with its piezoresistive response. Therefore, the electrical resistance change in the piezoresistive response is obtained by subtracting the temperature-dependent resistance from the total electrical resistance. The time-dependent transferred heat of the MWCNT/PDMS-composite/PDMS bimorph actuator on the PDMS layer is defined as

$$W = IV\Delta t, \tag{3}$$

$$Q_1 = \frac{\Delta T_1}{R_{th}}\Delta t = hA\Delta T_1 \Delta t, \quad (\Delta T_1 = T_{PDMS,t_n} - T_0), \tag{4}$$

$$Q_2 = \left(T_{PDMS}^4 - T_0^4\right)A\varepsilon\sigma\Delta t, \tag{5}$$

where I [A] is the current, V [V] is the applied voltage on the actuator, Δt [s] is the time defined as $(t_{n+1} - t_n,\ n \geq 0)$, R_{th} [K/W] is the thermal resistance, h [W/m^{2}K] is the heat transfer coefficient, A [m^2] is the surface area, T_{PDMS,t_n} [K] is the surface temperature of the PDMS at time t_n, T_0 [K] is the room temperature, ε is the emissivity of the PDMS, and σ [W/m^{2}K^4] is the Stefan–Boltzmann constant. The change in temperature of the PDMS layer is expressed by subtracting the heat transfer to air (Q_1) and the heat transfer by radiation (Q_2) from the Joule heat W of the MWCNT/PDMS composite layer:

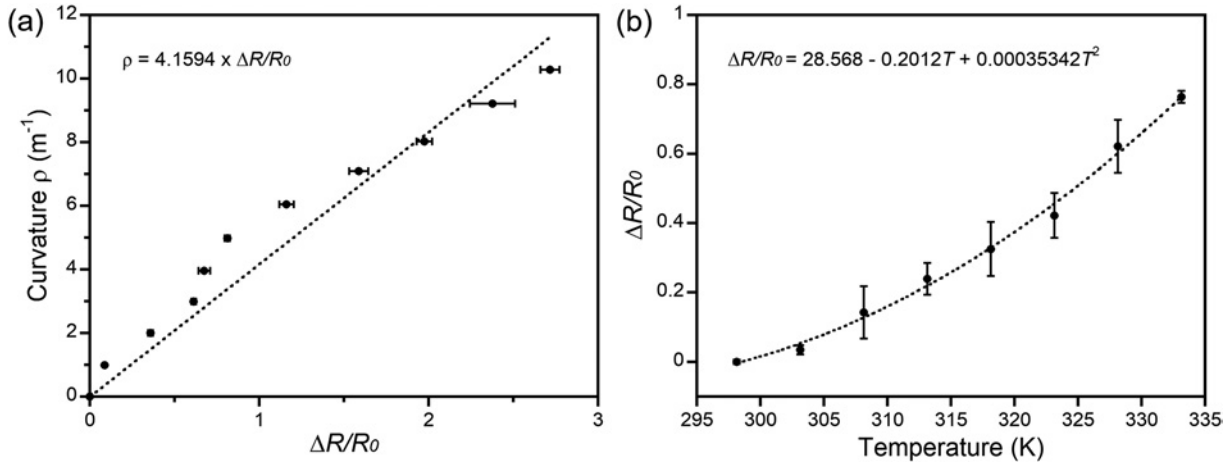

FIG. 4. (a) Curvature of bending sensor versus relative resistance. (b) Relative resistance of bending sensor for 298–333 K normalizing by the resistance at 298 K.

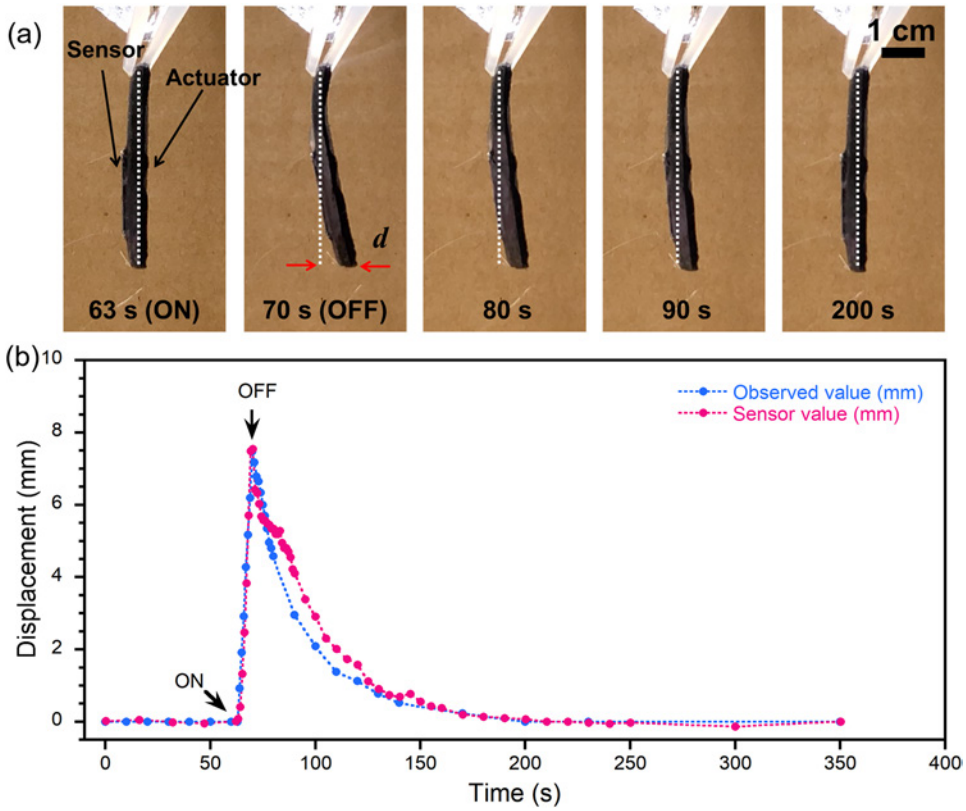

FIG. 5. (a) Optical images showing actuation process. (b) Comparison of displacement variation in camera monitoring and sensor feedback. Displacement variation of MWCNT/PDMS-composite/PDMS bimorph actuator with an applied DC voltage of 20 V and a current of 109.5 mA.

$$W - Q_1 - Q_2 = mc\Delta T \quad (\Delta T = T_{PDMS,t_{n+1}} - T_{PDMS,t_n}), \tag{6}$$

$$\Delta T = \frac{\Delta t}{mc}\left[IV - hA\Delta T_1 - \left(T^4_{PDMS,t_n} - T^4_0\right)A\varepsilon\sigma\right], \tag{7}$$

where m [g] is the mass of the PDMS and c [J/gK] is its specific heat capacity. From Eq. (7), we obtain the temperature transferred to the PDMS. Figure S5 compares the temperature variation by using the thermal camera and the calculation. The time-dependent temperature of the PDMS layer of the actuator shows a good correlation between the temperature obtained by the thermal camera and the calculation. Therefore, we obtain the temperature compensation from the electrical resistance change during actuation by subtracting Eq. (2).

Figures 5(a) and 5(b) show the self-sensing capability of the hybrid structure based on the actuator and the sensor. Figure 4(a) shows optical images of the actuation process of the MWCNT/PDMS-composite/PDMS bimorph actuator attached to the graphene-tubing bending sensor. The resulting bending was responsive to the Joule heat, indicating that the mechanism is as described above. A voltage of 20 V and a current of 0.195 A (i.e., a power of 2.19 W) were applied to drive the actuator for a time of 63 s, and the voltage was cut off at the time of 70 s as shown in Fig. 4(a). The maximum displacement was 7.55 mm, which is equivalent to a strain of 1.2% for the device. The driving power consumption was 1.05 mW/mm^3. When the voltage was applied, deformation was executed and the initial state was recovered after around 130 s (at the time of 200 s in the photograph) after the voltage was cut off. As shown in Fig. 4(b), the value of the displacement variation and the relative resistance changes of the sensor matches well with the actuator tip displacement collected from the captured photographs. However, a slight delay occurred when the power was switched off, this being due to the difference in the thermal conductivity between the composite of the actuator in the MWCNT/PDMS composite and the sensor in the graphene layers. Because we monitored the temperature only at the PDMS-layer side, the radiation heat at the MWCNT/PDMS composite was not taken in the account. Nevertheless, the dynamic motion of the actuator can be monitored directly through the input electric terminals and the sensory lead terminals, without any requirement for additional sensing components.

IV. CONCLUSION

In summary, we proposed an integrated device with a hybrid structure of an electrothermal actuator and a bending sensor with temperature-compensating ability, which can serve as a self-sensing system. The hybrid structure of the MWCNT/PDMS-composite/PDMS bimorph actuator and the hollow-tubing graphene-fiber bending sensor can provide simple operation and real-time sensing using a pair of input electric terminals and sensory lead-out terminals without additional image processing components. This proposed hybrid device will be useful for remote-sensing/operating devices.

SUPPLEMENTARY MATERIAL

See the supplementary material for the experimental details regarding preparing the actuator and sensors.

ACKNOWLEDGMENTS

This work was supported by the Japan Society for the Promotion of Science (JSPS), JSPSKAKENHI, Grant-in-Aid for Young Scientists (B) JP26870247, and Grant-in-Aid for Scientific Research (B) JP17H03402. Part of this research is based on the Cooperative Research Project of Research Center for Biomedical Engineering, Ministry of Education, Culture, Sports, Science and Technology (MEXT).

REFERENCES

[1] S. Kim, C. Laschi, and B. Trimmer, Trends Biotechnol. **31**, 287 (2013).
[2] D. Rus and M. Tolley, Nature **521**, 467 (2015).
[3] H. Zhao, K. O'Brien, S. Li, and R. Shepherd, Sci. Robotics **1**, eaai7529 (2016).
[4] T. Mirfakhrai, J. D. Madden, and R. H. Baughman, Mater. Today **10**, 30 (2007).
[5] P.-J. Cottinet, D. Guyomar, J. Galineau, and G. Sebald, Sensor. Actuat. A Phys. **180**, 105 (2012).
[6] L. J. Romasanta, M. A. Lopez-Manchado, and R. Verdejo, Prog. Polym. Sci. **51**, 188 (2015).
[7] D. Chen and Q. Pei, Chem. Rev. **117** (2017).
[8] H. So and A. Pisano, Microsyst. Technol. **21**, 195 (2015).
[9] J.-H. Jeong, T. Mun, H. Kim, J. Moon, D. Lee, R. Baughman, and S. Kim, Nanoscale Adv. **1**, 965 (2019).
[10] P. Xiao, N. Yi, T. Zhang, Y. Huang, H. Chang, Y. Yang, Y. Zhou, and Y. Chen, Adv. Sci. **3**, 1500438 (2016).
[11] N. Festin, C. Plesse, C. Chevrot, D. Teyssié, L. Josselin, P. Pirim, and F. Vidal, Proc. Comput. Sci. **7**, S4 (2011).
[12] L. Chen, M. Weng, Z. Zhou, Y. Zhou, L. Zhang, J. Li, Z. Huang, W. Zhang, C. Liu, and S. Fan, ACS Nano **9**, 12189 (2015).
[13] L. Z. Chen, C. H. Liu, C. H. Hu, and S. S. Fan, Appl. Phys. Lett. **92**, 263104 (2008).
[14] L. Chen, C. Liu, K. Liu, C. Meng, C. Hu, J. Wang, and S. Fan, ACS Nano **5**, 1588 (2011).
[15] Q. Li, C. Liu, Y. Lin, L. Liu, K. Jiang, and S. Fan, ACS Nano **9**, 409 (2015).
[16] Z. Zeng, H. Jin, L. Zhang, H. Zhang, Z. Chen, F. Gao, and Z. Zhang, Carbon **84**, 327 (2015).
[17] Z. Zhou, Q. Yan, C. Liu, and S. Fan, New Carbon Mater. **32**, 411 (2017).
[18] Q. Li, C. Liu, and S. Fan, Nanotechnol. **29**, 175503 (2018).
[19] H. Cheng, F. Zhao, J. Xue, G. Shi, L. Jiang, and L. Qu, ACS Nano **10**, 9529 (2016).
[20] H.-P. Phan, T. Dinh, T.-K. Nguyen, A. Vatani, A. Foisal, A. Qamar, A. Kermany, D. Dao, and N.-T. Nguyen, Appl. Phys. Lett. **110**, 144101 (2017).
[21] M. Amjadi and M. Sitti, Adv. Sci. **5**, 1800239 (2018).
[22] A. Nakamura, T. Hamanishi, S. Kawakami, and M. Takeda, Mater. Sci. Eng. B **219**, 20 (2017).
[23] B. Davaji, H. D. Cho, M. Malakoutian, J.-K. Lee, G. Panin, T. W. Kang, and C. H. Lee, Sci. Rep. **7**, 8811 (2017).